First-principles prediction of new stable 2D orthorhombic (o)-B_2CN and o-B_2C_2 materials for hydrogen storage applications via lithium decoration

Benaddi, Ayoub; Elomrani, Abdelali; Khossossi, Nabil; Maymoun, Mohammad; Oukahou, Said; Etrini, Ayoub; Hasnaoui, Abdellatif

DOI
10.1016/j.ijhydene.2025.03.389

Publication date
2025

Document Version
Final published version

Published in
International Journal of Hydrogen Energy

International Journal of Hydrogen Energy 127 (2025) 116–126

Contents lists available at ScienceDirect

International Journal of Hydrogen Energy

journal homepage: www.elsevier.com/locate/he

First-principles prediction of new stable 2D orthorhombic (o)-B_2CN and o-B_2C_2 materials for hydrogen storage applications via lithium decoration

Ayoub Benaddi [a,*], Abdelali Elomrani [b], Nabil Khossossi [c], Mohammad Maymoun [a], Said Oukahou [a], Ayoub Etrini [a], Abdellatif Hasnaoui [a]

[a] Sultan Moulay Slimane University of Beni Mellal, Polydisciplinary Faculty of Khouribga, LS2ME Laboratory, B.P. 145, 25000 Khouribga, Morocco
[b] Mohammed VI Polytechnic University (UM6P), Laboratory of Inorganic Materials for Sustainable Energy Technology (LIMSET), 43150 Benguerir, Morocco
[c] Department of Materials Science and Engineering, Delft University of Technology, Delft, The Netherlands

ARTICLE INFO

Keywords:
Hydrogen storage
2D materials prediction
o-B_2C_2 & o-B_2CN
Density functional theory

ABSTRACT

Nowadays, scientists are increasingly focused on finding new efficient 2D materials for hydrogen storage due to their large specific surface area, exceptional physisorption properties, and high gravimetric capacity. In this respect, we have analyzed the potential of new 2D orthorhombic (o)-B_2CN and o-B_2C_2 materials as lightweight solid mediums for hydrogen storage, employing lithium decoration through density functional theory (DFT) calculations. Both materials were found to be conductive and demonstrated excellent mechanical, dynamical and thermal stability. The binding energies of lithium adatoms to the monolayers during the decoration process were found to be −3.38 and −3.72 eV for o-B_2CN and o-B_2C_2, respectively. These values indicate strong interactions with both substrates and the lack of lithium clustering given that they are higher than its cohesive energy (−1.63 eV). The lithium decoration technique significantly improves the adsorption of H_2 molecules on both materials, where each system adsorbs 32 molecules with an average adsorption energy of 0.25 and 0.23 eV for $32H_2$@8Li-B_2CN and $32H_2$@8Li-B_2C_2, respectively, along with excellent gravimetric capacities of 12.87 and 13.29 wt% and desorption temperatures of 186 and 171 K. To assess dynamical stability, AIMD calculations were conducted on fully loaded H_2 systems at temperatures of 100, 200, 400 and 500 K, demonstrating complete H_2 desorption and confirming the reversibility of both systems. A radial distribution function (RDF) analysis was conducted to examine the thermal effects on Li–H atomic correlations and assess the stability of hydrogen adsorption at different temperatures. Based on these results, it can be concluded that Li-decorated o-B_2CN and o-B_2C_2 show considerable potential for hydrogen storage applications.

1. Introduction

The U.S. department of energy (DOE) fuel cell program supports research and development efforts focused on hydrogen and fuel cells, with the aim of promoting renewable energy sources for hydrogen generation while reducing the costs associated with storage and delivery. In this context, 2D materials have emerged as a promising approach to enhance hydrogen storage systems, particularly for onboard fuel cells [1–3]. These materials offer several advantages over traditional hydrogen storage materials, such as complex hydrides and nanostructured metal hydrides [2], which primarily rely on chemisorption, offer high storage capacities and adsorption energies due to the formation of strong covalent bonds between hydrogen molecules and the storage medium. However, this method presents significant challenges, including the need for extremely high desorption temperatures and slow hydrogen absorption rates, which limit their practical utility, particularly in onboard systems [4]. In contrast, 2D materials offer a more promising alternative by utilizing physisorption, where hydrogen molecules are adsorbed through weak van der Waals interactions. This approach not only allows for reversible hydrogen adsorption but also facilitates easier and more efficient release of stored hydrogen, making 2D materials more suitable for practical hydrogen storage applications, especially in fuel cell technologies [5]. With their structural diversity, large specific surface area, lightweight properties, improved storage efficiency, and safety, 2D materials present a compelling solution for advanced hydrogen storage applications [6–14].

Owing to these advantages, many 2D materials have garnered significant attention, with numerous candidates being either theoretically predicted using advanced computational methods or experimentally synthesized, including examples such as graphene [15], silicene [16], germanene [17], and stanene [18], as well as borophene and its

* Corresponding author.
E-mail address: ayoub.benaddi@usms.ma (A. Benaddi).

https://doi.org/10.1016/j.ijhydene.2025.03.389
Received 23 November 2024; Received in revised form 7 February 2025; Accepted 28 March 2025
Available online 12 April 2025

polymorphs [19], which are particularly known for their excellent hydrogen adsorption properties and, most importantly, their lightweight nature owing to their relatively high gravimetric capacity. In this context, many researchers have attempted to combine boron atoms with other lightweight elements, particularly those from groups III, IV, and V of the periodic table, to develop new 2D materials with promising adsorption properties, especially with regard to their lightweight nature. Among these materials, we can refer to boron nitride (BN), known as "white graphene" [20], boron phosphide (BP) [21], boron carbide (BC) [22], boron hydride (BH) [23], boron arsenide (BAs) and boron silicon (BSi) [24–26].

A novel class of orthorhombic two-dimensional allotropes has recently been identified through first-principles calculations, comprising boron atoms combined with elements from Groups IV and V of the periodic table, represented by the formula B_2X_2 (where X signifies these group elements) [24]. The orthorhombic arrangement of B_2X_2 showcases a distinctive alteration of the well-established hexagonal graphene-like structure, revealing exceptional properties that set it apart from conventional two-dimensional materials. In this configuration, the boron and X atoms establish a network reminiscent of the honeycomb lattice of graphene; however, the slight distortion inherent in the orthorhombic lattice and the new alternation of atoms, introduces innovative anisotropic, electronic, optical and mechanical attributes to the material [27]. Notably, these compounds have demonstrated significant hydrogen adsorption capabilities, with high capacities observed in materials such as orthorhombic boron nitride (o-B_2N_2), orthorhombic boron phosphide (o-B_2P_2), and orthorhombic boron silicon (o-B_2Si_2), exhibiting hydrogen storage capacities of 9.7 wt%, 8.18 wt%, and 8.1 wt%, respectively [5,25].

In this context, we aim to study for the first time the properties of o-B_2C_2 and o-B_2CN monolayers and their application as hydrogen storage media. Motivated by the synthesis of 2D boron nitride (h-BN) and recent synthesis of 2D h-BCN material by Beniwal et al. and Ajayan et al. [20,28,29] which have garnered significant interest due to their ability to integrate the advantageous properties of both h-graphene and h-BN structures, we conducted a thermodynamic analysis of o-B_2C_2 and o-B_2CN, revealing that these materials have the potential to be synthesized in their orthorhombic form.

To enhance the interaction between hydrogen molecules and the surface, we adopt a lithium decoration strategy. Given that the van der Waals interactions between H_2 molecules and the surface are relatively weak, this approach aims to strengthen these interactions, thereby improving the overall hydrogen adsorption capacity [30–34]. The selection of lithium as an intermediate is primarily driven by its low atomic mass compared to other alkali, alkaline earth, and transition metals. This minimal mass contribution helps maintain the host material's overall weight, thereby enhancing its gravimetric capacity. Additionally, lithium exhibits a significantly higher binding energy-to-cohesive energy ratio than heavier elements like Ti, Pd, Pt, and Sc, which reduces the likelihood of cluster formation.

Building on these recent theoretical and experimental advancements, this paper investigates the potential of o-B_2C_2 and o-B_2CN monolayers as solid media for hydrogen storage using density functional theory (DFT) calculations. We first examined the structural, mechanical, and electronic properties of both materials, confirming their dynamic and thermal stability through phonon dispersion and ab initio molecular dynamics (AIMD) studies. Subsequently, a lithium atom decoration strategy was applied to the o-B_2C_2 and o-B_2CN monolayers, and the adsorption behavior of H_2 molecules on the decorated surfaces was explored. Finally, we assessed the hydrogen storage capacities and desorption temperatures of these systems, and further investigated the desorption processes of H_2 molecules at various temperatures through AIMD calculations. Furthermore, we performed a radial distribution function (RDF) analysis to investigate hydrogen desorption, focusing on how temperature impacts Li–H atomic correlations and the stability of hydrogen adsorption at different thermal conditions.

2. Computational details

All calculations were conducted using density functional theory (DFT) within the projector augmented wave method [35,36], as implemented in the Quantum Espresso software [37,38]. The exchange–correlation interactions were estimated using the Perdew–Burke–Ernzerhof (PBE) generalized gradient approximation [39,40]. To effectively address the challenges posed by dispersion interactions, our studies incorporated the van der Waals-corrected DFT (DFT-D2) method, as introduced by Grimme [41,42]. Force convergence criteria were established at 10^{-3} eV/Å and energy convergence criteria at 10^{-6} eV. In addition, during the calculations, the cutoff values for kinetic energy in handling wave functions and charge density were fixed at 1020 eV (≈ 75 Ry) and 10200 eV (≈ 750 eV), respectively. Moreover, we used optimized 8 × 16 × 1 and 4 × 8 × 1 k-point mesh for Brillouin zone sampling for both unit cells and supercells, respectively, for B_2C_2 and B_2CN monolayers, and we introduced a 20 Åvacuum along the *z*-axis to reduce inter-layers interactions.

Furthermore, ab-initio molecular dynamics (AIMD) simulations of the canonical ensemble (NVT) were performed to check the thermal stability of the studied monolayers with a total calculation time of 9 ps for 2 × 4 × 1 and 5.5 ps for 4 × 6 × 1 super-cells with an integration step of 1 fs at a temperature of 300 K. To examine the dynamic stability, the vibrational phonon spectrum was calculated using the finite displacement approach included in the PHONOPY code [43].

To evaluate the energetic stability of both systems, the cohesive energy was calculated using the following equation:

$$E_c = -\frac{E_{\text{system}} - \sum_i n_i E_i}{4} \tag{1}$$

in which E_{system} and E_i represent, respectively, the total energy of the unit cell for each monolayer and the energy of free atoms calculated by isolating each single atom type i in a cubic system with a cell parameter of 20 Å in a manner that eliminates unwanted periodic interactions and ensures an accurate calculation of total energy. n_i is the number of atoms of type i (B, C or N).

The adsorption energy of a Li-adatom on the diboron dicarbide/carbon nitride monolayer was computed according to the following equation:

$$E_b = \frac{E_{system} + kE_{Li} - E_{system+Li}}{k} \tag{2}$$

in which $E_{system+Li}$, E_{system}, and E_{Li}, respectively, denote the total energies of lithium-decorated system, pristine system, and the isolated lithium atom. k is the number of lithium atoms.

To describe the interaction that occurs between Li atoms and possible active sites of substrate, the charge density difference was computed according to the formula :

$$\Delta\rho = \rho(Li + system) - \rho(system) - \rho(Li) \tag{3}$$

where $\rho(Li + system)/\rho(system)$ is the charge density of the system with/without Li decoration, respectively. $\rho(Li)$ is the charge density of a single Li-adatom. The last two densities were calculated with the same cell parameters and atomic positions of the decorated system.

The adsorption energy of hydrogen molecules on Li-decorated systems was calculated using the following equation:

$$E_{ad} = \frac{E_{kLi@system} + nE_{H_2} - E_{nH_2/kLi@system}}{n} \tag{4}$$

where $E_{kLi@system}$, E_{H_2}, and $E_{nH_2/kLi@system}$ are the total energy of a Li-decorated system, the total energy of an isolated H_2 molecule, and energy of n hydrogen molecules (nH_2) adsorbed on a Li-decorated o-B_2C_2 and o-B_2CN monolayers, respectively.

Besides, the gravimetric capacity (wt%), which is a critical factor for any hydrogen storage system, was evaluated using the following expression:

$$C\ (wt\%) = \frac{M_T(H_2)}{M_T(\text{system})} \times 100 = \frac{nM(H_2)}{nM(H_2) + kM(Li) + M(host)} \times 100 \tag{5}$$

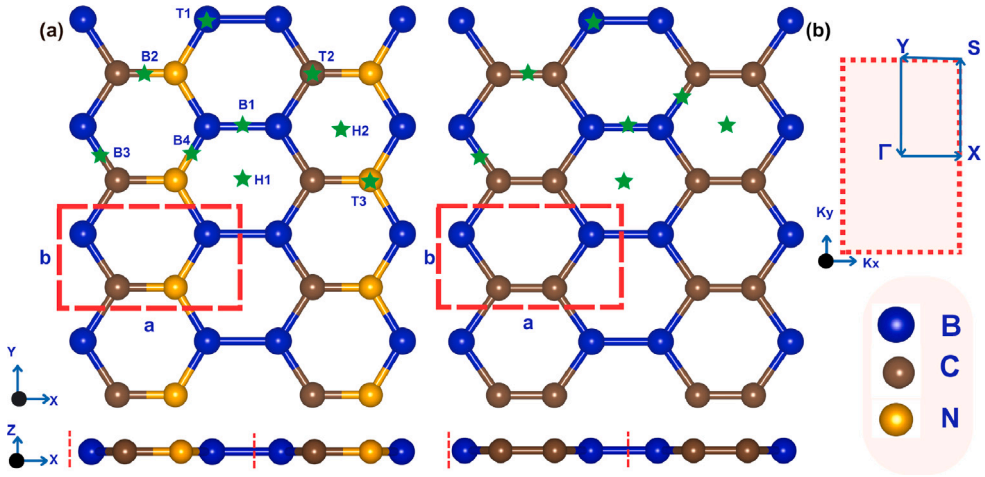

Fig. 1. (a) Top and side views of the optimized structures of (2 × 4 × 1)-supercell of orthorombic (o-) B_2CN and B_2C_2 monolayers. The red dashed rectangle refers to the unit cell and the green stars indicate the possible adsorption sites. The blue, brown and yellow spheres represents the B, C and *N* atoms in III, IV and V columns of periodic table, respectively. (b) The first Brillouin zone of the unit cell with a path connect the high symmetry points in k-space, *Γ*–X–S–Y–*Γ*. (For interpretation of the references to color in this figure legend, the reader is referred to the web version of this article.)

where n and k represent the number of H_2 molecules and Li atoms, respectively, and M stands for their respective molar masses [44].

Furthermore, to discuss the reversibility of the hydrogen molecules uptake and release procedure, we have estimated the desorption temperature of hydrogen molecules (T_D) using the van't Hoff formula:

$$T_D\,(K) = \left(\frac{E_{ad}}{K_B}\right)\left(\frac{\Delta S}{R} - Ln(P)\right)^{-1} \quad (6)$$

Where E_{ad} is the average energy of adsorption, K_B is the Boltzmann constant, ΔS (130 $Jmol^{-1}K^{-1}$) represents the variation in H_2 entropy from molecular gas to dissolved solid hydrogen [45], R = 8.314 $Jmol^{-1}K^{-1}$, is the universal gas constant, and P is the equilibrium pressure P = 1 atm.

3. Results and discussion

3.1. Structure, stability and electronic properties

Fig. 1(a) displays the optimized atomic structure of a 2 × 4 × 1 supercell of orthorhombic (o-) B_2C_2 (diboron dicarbide) and B_2CN (diboron carbon nitride) monolayers after full relaxation. The Primitive cell represented by the red dashed rectangle, includes two boron and carbon atoms for diboron carbide, whereas the unit cell of diboron carbon nitrogen consists of two boron atoms, one carbon atom and one nitrogen atom.

Both 2D monolayers exhibit a planar structure and belong to the orthorhombic crystal system; however, they differ in their space groups: B_2C_2 belongs to Pmmm (no. 47), while B_2CN belongs to Pmm2 (no. 25). The B_2C_2 monolayer can be considered as a novel boron-carbon (BC) polymorph with an orthorhombic structure, formed by rearranging the hexagonal (h)-BC atoms [22,46,47]. In contrast, B_2CN can be regarded as a polymorph belonging to the BCN family [48–50].

Furthermore, we conducted a comparison of structural parameters between both materials and other orthorhombic structures from groups III, IV, and V within the primitive cell. The optimized lattice constants a and b, along with the bond lengths between atoms, are detailed in Table 1. As can be deduced, the size of the primitive cell will vary due to the atomic radii of different atoms, which increase progressively with C, N, B, P, Al, and As atoms.

To investigate the theoretical stability and verify the feasibility of experimental synthesis for these new 2D materials, our first step was to evaluate the thermodynamic stability through the calculation of cohesive energy as described in Eq. (1). The findings reveal a cohesive energy of 6.02 and 6.53 eV per atom for B_2C_2 and B_2CN monolayers, respectively, demonstrating the robustness of the atomic bonds in these systems and ensuring their structural stability. Furthermore, the calculated cohesive energies are relatively close to those of synthesized materials such as graphene (7.46 eV per atom) and BN (6.60 eV per atom) [52,53], and more higher than other 2D materials such as Mg_2C (3.43 eV/atom), Mn_2C (3.35 eV/atom), Be_2C (4.86 eV/atom) and phosphorene (3.71 eV/atom) [54–57].

In the next step, we assessed the dynamic stability of the two monolayers by plotting the phonon dispersion curves along the high-symmetry path in the first Brillouin zone (*Γ*–X–S–Y–*Γ*), as depicted in Fig. S1 in (SM). The lack of imaginary frequencies confirms the dynamical stability of the o-B_2C_2 and o-B_2CN structures, highlighting their potential for various applications. Furthermore, to elucidate the mechanical properties of our two anisotropic materials, we computed the elastic constants, Young's modulus, and Poisson's ratio along the x- and *y*-directions using the energy vs strain method, with strain ranging from −0.03 to 0.03 in increments of 0.005. Table 2 presents the calculated results and compares our materials with other monolayers of the same crystal structure. As shown in the table, the calculated elastic constants satisfy the criteria for mechanical stability, which necessitates: $C_{11} > 0$, $C_{22} > 0$, $C_{66} > 0$ and $C_{11}.C_{22} - C_{12}^2 > 0$. Additionally, the higher elastic constants and Young's moduli of o-B_2C_2 and o-B_2CN suggest that these materials are more rigid and resistant to deformation compared to o-B_2P_2 [58] and o-Al_2N_2 [51] and the higher C_{66} elastic constant of o-B_2CN compared to o-B_2C_2 indicates better resistance to shear deformation.

Finally, we checked the stability of the (2 × 4 × 1) and (4 × 4 × 1) super-cells of o-B_2C_2 and o-B_2CN monolayers at a temperature of 300 K using ab initio molecular dynamics (AIMD) simulations, with time durations of 9 ps and 5.5 ps, respectively, and a time step of 1 fs. As can be seen from Fig. S2 in (SM), the total energy exhibits minimal variation over time, and it is observed that no bonds are broken within both structures. These findings confirm the stability of the o-B_2C_2 and o-B_2CN monolayers, which makes them potential materials for various applications and gives us the motivation for further investigation into their capability as hydrogen storage media.

We examined the electronic properties of o-B_2C_2 and o-B_2CN monolayers by plotting the band structures calculated using the GGA-PBE functional, as presented in Fig. 2(a) and (b). As shown in the figure, the orthorhombic o-B_2C_2 and o-B_2CN monolayers exhibit metallic characteristics and a Dirac cone is observed above the Fermi level along the high-symmetry Y–*Γ* direction in o-B_2C_2. In contrast, this

Table 1
The structural parameters of the 2D o-B_2C_2 and o-B_2CN materials compared to other orthorhombic structures from group III ≡ B, Al; IV ≡ C and V ≡ N, P, As. *a* and *b* are the lattice constants, *d* is the bond length and E_{coh} is the corresponding cohesive energy.

System	o-B_2C_2	o-B_2CN	o-B_2N_2 [5]	o-B_2P_2 [5]	o-B_2As_2 [24]	o-Al_2N_2 [51]
a(Å)	4.83	4.66	4.57	5.61	5.91	5.92
b(Å)	2.60	2.56	2.50	3.24	3.40	3.15
$d_{III-III}$(Å)	1.67	1.69	1.70	1.65	1.63	2.54
d_{IV-IV}(Å)	1.35	–	–	–	–	–
d_{V-V}(Å)	–	–	1.44	2.13	2.34	1.47
d_{III-IV}(Å)	1.58	1.52	–	–	–	–
d_{III-V}(Å)	–	1.49	1.44	1.86	1.96	1.82
d_{IV-V}(Å)	–	1.38	–	–	–	–
E_{Coh}(eV)	6.02	6.53	6.23	4.80	–	5.59

Table 2
A comparative analysis of the elastic constants (C_{11}, C_{12}, C_{22}, and C_{66}) as well as Young's modulus and Poisson's ratio along x- and y-directions of (2D) o-B2C2 and o-B_2CN compared with other orthorhombic monolayers.

System	C_{11} (N/m)	C_{12} (N/m)	C_{22} (N/m)	C_{66} (N/m)	$Y_x - Y_y$ (N/m)	$V_x - V_y$
o-B_2C_2	291.50	41.10	173.02	97.13	281.74 – 167.23	0.24 – 0.14
o-B_2CN	263.24	51.94	209.13	105.4	250.34 – 198.80	0.25 – 0.20
o-B_2N_2 [59]	250.39	35.11	291.65	21.98	246.17 – 286.73	0.12 – 0.14
o-B_2P_2 [58]	154.40	34.70	135.70	49.60	145.53 – 171.12	0.26 – 0.22
o-Al_2N_2 [51]	145.12	28.59	143.80	44.38	143.00 – 141.00	0.19 – 0.19

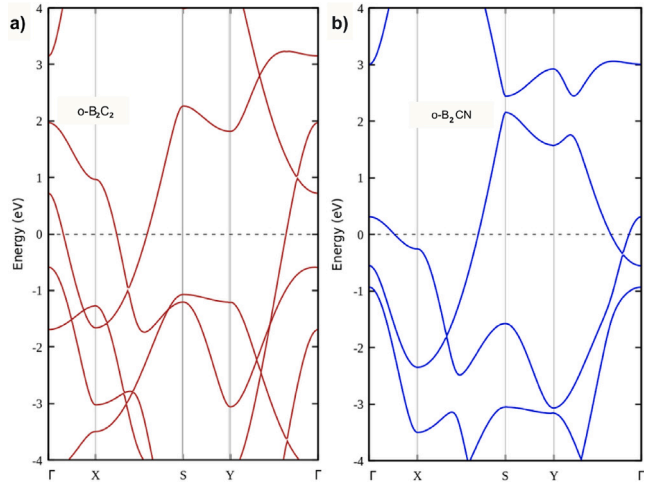

Fig. 2. Projected band structure of (a) o-B_2C_2 and (b) o-B_2CN monolayers, calculated using the DFT-PBE functional.

cone shifts below the Fermi level in the o-B_2C_2 monolayer, which can be attributed to the higher electron count in the *N* atom compared to the C atom. Additionally, there are significantly more available bands above the Fermi level in o-B_2C_2 than in the o-B_2CN monolayer, strongly indicating that o-B_2C_2 has superior electronic conductivity. It is noteworthy that the diboron dinitrogen monolayer o-B_2N_2 [5] behaves as a semiconductor with a finite band gap, suggesting that the total or partial substitution of *N* with C could significantly enhance the electronic properties.

Moreover, we plotted the partial density of states (PDOS) for the o-B_2C_2 and o-B_2CN monolayers in Fig. S3 in (SM). As shown, the p-orbitals of B, N, and C atoms primarily contribute to the bands across the Fermi level. The s-orbitals either lie below the Fermi level, as observed in o-B_2C_2, or have a negligible contribution at the Fermi level, as seen in o-B_2CN. Additionally, a strong overlap between the p-orbitals indicates covalent bonding between the atoms. Similar to the band structure, the density of states at the Fermi level in o-B_2C_2 is higher than in o-B_2CN, and it begins to decrease in the latter. This suggests that o-B_2C_2 may exhibit better electronic conductivity compared to its counterpart.

3.2. Single H_2 adsorption and lithium decoration of o-B_2C_2 and o-B_2CN monolayers

We initiated the hydrogenation process by positioning a single molecule in different orientations at the adsorption sites of o-B_2C_2 and o-B_2CN monolayers. As illustrated in Fig. 1, the o-B_2CN structure offers nine potential adsorption sites, including two hollow sites (H1 and H2 hexagons), four bridges (B1, B2, B3 and B4 for B–B, C–N, B–C and B–N bonds) and three top of atoms sites (T1, T2 and T3 for the top of B, C and *N* atoms) while the o-B_2C_2 structure offers only seven adsorption sites due to the symmetry change with two substituted carbon atoms, it still includes two hollow sites (H1 and H2 hexagons), along with three bridge sites (B1, B2, and B3 for B–B, C–C and B–C bonds) and two top sites (T1 and T2 for the top of B and C atoms). After a full optimization of the H_2 molecule on both systems as shown in Fig. S4 in (SM), we found that the H1-site is the most favorable site, with adsorption energies of 0.058 and 0.048 eV and distances of 2.6 and 2.4 Å for o-B_2CN and o-B_2C_2, respectively. These calculated adsorption energies fall outside the proposed range of 0.17–0.6 eV, indicating that the H_2 molecule has not been effectively adsorbed due to its weak interaction with the monolayers [21].

To overcome this limitation, we adopted a lithiation strategy to enhance the reactivity of both surfaces during the adsorption of hydrogen molecules. Furthermore, the choice of lithium is based on the fact that it is the lightest metal element in the periodic table, ensuring that it does not significantly increase the overall weight of the system, thus preventing a decrease in gravimetric capacity [60].

Consequently, we studied the adsorption of a single lithium adatom at each previously mentioned site. Using Eq. (2), we calculated the binding energies, as presented in Table S1, and as it can be observed, the minimal binding energy corresponds to the Hollow (H1) site, indicating that the lithium adatom prefers to be adsorbed at the center of the H1 hexagon for both materials, as shown in Fig. 3 . The calculated binding energies were found to be 3.38 eV and 3.72 eV for o-B_2CN and o-B_2C_2 systems, respectively, which are significantly higher than the cohesive energy of a lithium atom (1.63 eV), indicating also the absence of lithium clustering [61]. Furthermore, it can be deduced that both materials exhibit exceptional reactivity to lithium compared to other 2D monolayers such as o-B_2N_2 (−1.98 eV) [5], o-B_2P_2 (−3.09 eV) [5], borophene (−3.28 eV) [62], carbon nitride (−2.8 eV) [63], black phosphorus (−1.8 eV) [64], germanene (−2.18 eV) and silicene (−2.6 eV) [65,66].

To gain a more comprehensive understanding of the interaction between Li adatom in most favorable site of surfaces, we utilized Eq. (3)

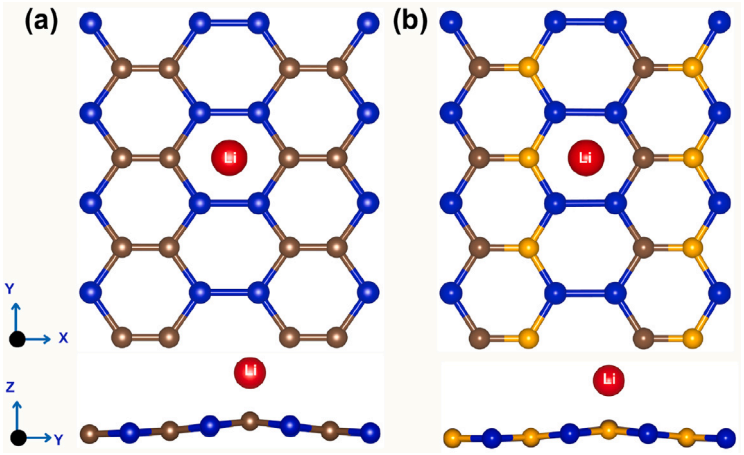

Fig. 3. (a) and (b) Top and side views of single Li adatom adsorption at the hollow site of o-B_2C_2 and o-B_2CN monolayers, respectively.

Table 3
Binding energies (E_b) of the two systems decorated with varying lithium amounts, along with the lithium-to-substrate distances ($d_{Li\text{-}system}$), the minimum lithium-to-lithium distances ($d_{Li\text{-}Li}$) between neighboring adsorbents, and corresponding charge transfer values.

System	E_b (eV)	$d_{Li-system}$ (Å)	d_{Li-Li} (Å)	Charge $\|e\|$
1Li@B_2C_2	−3.72	1.56	9.65	0.90
1Li@B_2CN	−3.38	1.58	9.30	0.89
2Li@B_2C_2	−3.72	1.53	4.35	0.89
2Li@B_2CN	−3.34	1.58	4.33	0.89
4Li@B_2C_2	−3.58	1.64	4.27	0.89
4Li@B_2CN	−3.16	1.62	4.29	0.88
8Li@B_2C_2	−3.47	1.70	4.16	0.87
8Li@B_2CN	−3.02	1.72	4.17	0.86

to calculate the spatial distribution of the charge density difference for both Li@B_2CN and Li@B_2C_2 systems, as illustrated in Fig. 4. As observed, there is a charge accumulation between the Li adatom and the hollow site (indicated by the yellow color), while the top of the Li atom is surrounded by an electron depletion zone (shown in blue). This suggests a net charge transfer (≈ 90%) from the Li adatom to B_2CN and B_2C_2 surfaces, given the lower electronegativity of B, C, and *N* atoms relative to lithium.

Following the adsorption of a single lithium, we gradually increased the number of Li adatoms. To achieve the most stable Li-surface configurations with minimal energy, we examined all possible arrangements on both sides involving 2, 4, and 8 adatoms (saturated system). Additionally, by maintaining appropriate distances between the lithium atoms, we aimed to minimize the steric effect, which could otherwise lead to unwanted interactions, such as clustering. The most energetically favorable configurations are depicted in Fig. S5 in (SM), along with their calculated binding energies. As it can be seen from the figure, lithium atoms have been adsorbed in an interlaced configuration on both materials, consistent with their adsorption on o-B_2P_2 monolayer, however, this differs from o-B_2N_2, which exhibits a preference for vertical lithium atom adsorption [5]. The binding energy of the fully saturated lithium structures, 8Li@B_2C_2 and 8Li@B_2CN was found to be −3.47 and −3.02 eV, respectively. These values are significantly greater than the Li-cohesive energy (1.63 eV), indicating the lack of Li-clustering in this configuration. Furthermore, it is noteworthy that the calculated binding energy of B_2C_2 is higher than that of B_2P_2 and B_2N_2 while B_2CN has a higher binding energy than B_2N_2 but is slightly lower than that of B_2P_2 [5]. This comparison underscores the differing reactivity of each substrate towards lithium, even among materials that share the same structure. Table 3 presents the binding energies for different percentages of lithium on the monolayers, along with the Li–Li distances and the Li–substrate distances. It also provides the charge transfer from the Li atoms to the monolayer at various concentrations, which clearly decreases as the number of adatoms increases.

3.3. Hydrogen adsorption onto Li-decorated B_2C_2 and B_2CN monolayers

As previously indicated, the decoration of the system's surface with lithium atoms at varying concentrations remains one of the most effective methods for enhancing the adsorption of H_2 molecules through polarization [67]. The lithium adatoms, characterized by positive charges, and the negatively charged substrates generate an electric field that polarizes and systematically arranges the hydrogen molecules around the Li adatoms [21]. In this context, we initiated our study by adsorbing a single H_2 molecule on Li@B_2C_2 and Li@B_2CN systems, exploring various placements to identify the most stable configurations. Following the same approach, we gradually increased the number of adsorbed H_2 molecules to a maximum of four (see Fig. 5).

Using Eq. (3), we calculated the adsorption energy for each configuration, which is detailed in Table 4, along with the H–H bond lengths, the distances between Li and H_2 molecules, and the corresponding gravimetric capacity. The average hydrogen adsorption energy for single H_2 molecule was found to be 0.27/0.29 eV for Li@B_2C_2/Li@B_2CN, and 0.21/0.22 eV for four adsorbed H_2 molecules. This decrease in energy can be attributed to the repulsive forces between the H_2 molecules, as each adsorbed molecule exerts pressure on its neighboring molecules in an attempt to achieve an optimal configuration. As observed in the table, the distance between Li atom and the H_2 molecules increases with the addition of more molecules, which results from the weakening interaction between Li and H_2, gradually affecting the adsorption energy. Additionally, the H–H bond lengths across all configurations range from 0.751 to 0.757 Å, confirming that the H_2 adsorption occurs via physisorption rather than chemisorption process. Consequently, the captured H_2 molecules remain in a non-dissociative form [68], unlike the Kubas effect and spillover mechanisms, typically involve the use of transition metals as catalysts, which significantly modify the electronic state of the H_2 molecule, affecting its binding dynamics and energy profile on the surface.

Next, and by decorating both sides with two lithium adatoms, we studied the adsorption of hydrogen molecules on the 2Li@B_2C_2 and

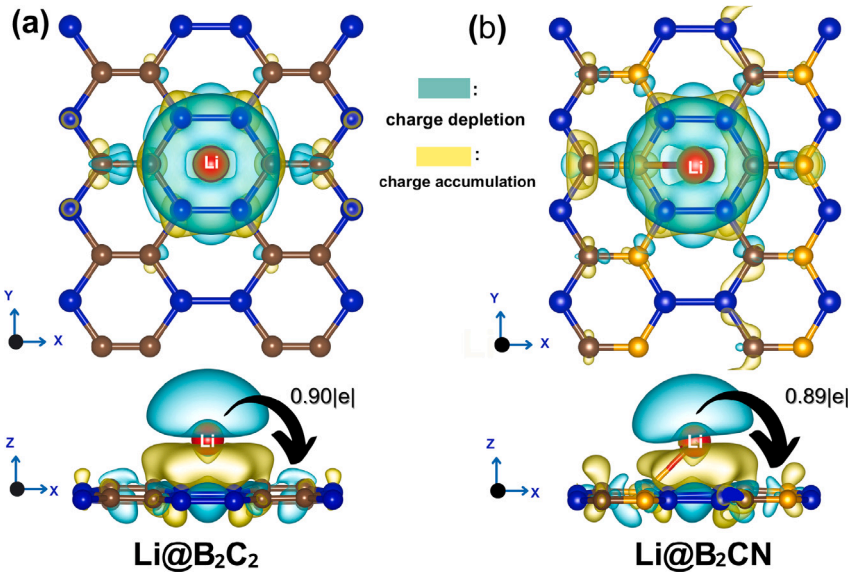

Fig. 4. (a) and (b) Top and side views of the isosurface charge density plots for the 1Li@B_2C_2 and 1Li@B_2CN systems with isosurface values of 6.6×10^{-4} and 1.0×10^{-3} e.Å^{-3}, respectively. (For interpretation of the references to color in this figure legend, the reader is referred to the web version of this article.)

Table 4
The calculated adsorption energy (E_{ad}) values for nH_2 (where n = 1, 2, 3, and 4) on the 1Li@B_2CN and 1Li@B_2C_2 monolayers are presented. The average H–H bond length is denoted as d_{H-H}, while d_{Li-H2} refers to the distance between the H_2 molecules and the lithium atoms. C_g indicates the gravimetric capacity.

System	$E_{ad}(eV/H_2)$	d_{H-H}(Å)	d_{Li-H_2}(Å)	C_g(wt%)
1H_2-1Li@B_2CN	−0.29	0.75	1.96	0.51
2H_2-1Li@B_2CN	−0.27	0.76	1.96	1.02
3H_2-1Li@B_2CN	−0.25	0.75	1.97	1.53
4H_2-1Li@B_2CN	−0.22	0.75	2.03	2.03
1H_2-1Li@B_2C_2	−0.27	0.76	1.94	0.53
2H_2-1Li@B_2C_2	−0.27	0.75	1.94	1.07
3H_2-1Li@B_2C_2	−0.25	0.75	1.96	1.59
4H_2-1Li@B_2C_2	−0.21	0.75	2.03	2.12

2Li@B_2CN systems. The calculated hydrogen adsorption energy decreases from 0.29 eV for 1H2–2Li@B_2CN to 0.22 eV for 4H2–2Li@B_2CN. Similarly, the adsorption energy decreases from 0.27 eV for 1H2–2Li@B_2C_2 to 0.21 eV for 4H2–2Li@B_2C_2 which confirms the previous analysis that we provided.

Finally, we have adsorbed hydrogen molecules on the 8Li@B_2C_2 and 8Li@B_2CN systems, which represent the maximum lithium-decorated monolayers on both sides. As depicted in Fig. 6, both systems can adsorb up to 32 H_2 molecules, resulting in a gravimetric capacity of 12.87 wt% for 32H2-8Li@B_2CN and 13.29 wt% for 32H2-8Li@B_2C_2, with an adsorption energy of 0.20 eV. These capacity values are significantly higher than those of other comparable 2D Li-functionalized materials, such as graphene, phosphorene, and hexagonal boron phosphide (h-BP), which exhibit capacities of 7.26, 4.4, and 7.40 wt%, respectively [21,69,70]. Additionally, the capacities of the studied materials are comparable to that of t-B_4N_4, which has a capacity of 12.47 wt% [60].

Table 5 presents the adsorption energy for full adsorbed H_2 molecules on one, four and eight lithium configuration, along with the H–H bond lengths, the distances between the Li atoms and the H_2 molecules, and the corresponding gravimetric capacity.

The difference in gravimetric capacity is evidently due to the variation in the molar mass of the nitrogen atom relative to that of carbon, which affects the total mass of the host material and thereby directly impacts the gravimetric capacity calculated using Eq. (6), this result underscores the selection of lightweight materials composed of B, C, and *N* atoms, further enhanced by decoration with lightweight alkali metals. Meanwhile, the difference in the average adsorption energy can be attributed to the variation in electronegativity between nitrogen (3.00) and carbon (2.55), along with the superior hydrogen adsorption properties of nitrogen compared to carbon [71].

Furthermore, the calculated average adsorption energy was found to be 0.25 eV for the fully decorated o-B_2CN and 0.23 eV for o-B_2C_2. These findings fall within the adsorption energy range [0.17–0.60 eV] suggested by the DOE, highlighting the effectiveness of the lithium decoration strategy compared to the use of non-decorated pristine monolayers. Furthermore, the results exceed those reported for Li-functionalized 2D o-B_2N_2, o-B_2P_2 and o-B_2Si_2 materials, which share the same orthorhombic crystalline structure, with average adsorption energies of 0.20, 0.18 and 0.14 eV, respectively [5,25]. This highlights the enhanced hydrogen storage potential of the predicted materials compared to these systems. In addition, the adsorption energies found in this study are higher than those of lithium-decorated t-graphene-like 2D boron nitride (0.21 eV) and hexagonal boron phosphide (0.19 eV) [21,60].

Fig. 7 provides a comparison of the gravimetric capacity and average adsorption energy of the studied Li-functionalized monolayers relative to other 2D Li-functionalized materials. As shown in this figure, the two materials are well-positioned, with capacities exceeding DOE standards and adsorption energies falling within the optimal range. The notable improvement in capacity and adsorption energy positions the studied materials as strong candidates for hydrogen storage applications.

Moreover, it is well established that the desorption temperature is a critical factor in assessing the reversibility of the hydrogen molecule uptake and release process. To determine this parameter, we utilized the van't Hoff formula given in Eq. (6). The resulting theoritical desorption temperatures were found to be 186 and 171 K for a 32 H_2

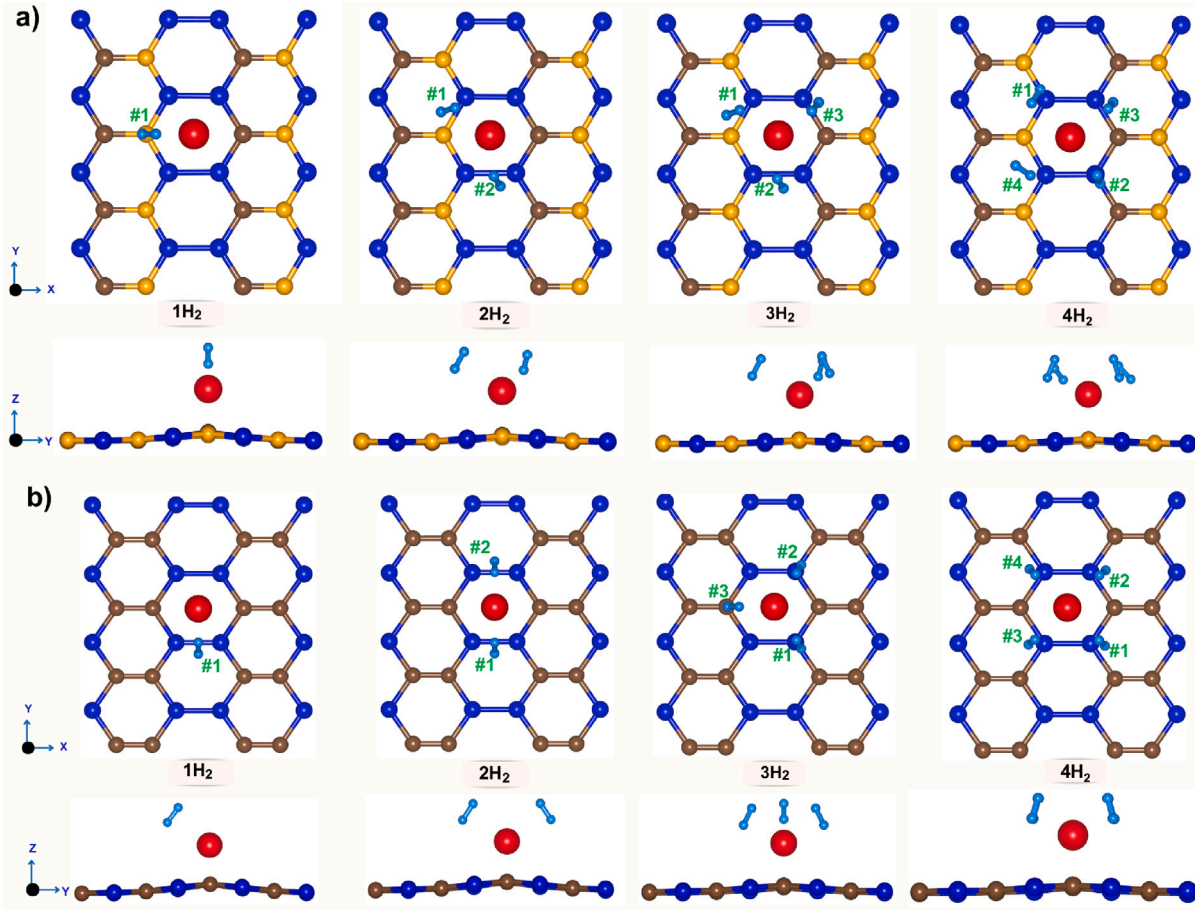

Fig. 5. (a) and (b) Optimized structures of Li-decorated o-B_2CN and o-B_2C_2 monolayers, showing the progressive adsorption of hydrogen molecules ranging from $1H_2$ to $4H_2$, respectively.

Table 5
The calculated adsorption energy (E_{ad}) values for nH_2 (where n = 4, 8, and 32) on $kLi@B_2CN$ and $kLi@B_2C_2$ monolayers, with k = 1, 2, and 8. The average H–H bond length is denoted as d_{H-H}, while d_{Li-H2} refers to the distance between the H_2 molecules and the lithium atoms. C_g indicates the gravimetric capacity.

System	$E_{ad}(eV/H_2)$	d_{H-H}(Å)	d_{Li-H_2}(Å)	C_g(wt%)
$4H_2$-$1Li@B_2CN$	−0.22	0.75	2.05	2.030
$4H_2$-$1Li@B_2C_2$	−0.21	0.75	2.03	2.120
$8H_2$-$2Li@B_2CN$	−0.22	0.75	2.07	3.560
$8H_2$-$2Li@B_2C_2$	−0.21	0.75	2.03	3.690
$32H_2$-$8Li@B_2CN$	−0.20	0.76	2.20	12.87
$32H_2$-$8Li@B_2C_2$	−0.20	0.76	2.24	13.29

adsorbed molecules on o-B_2CN and o-B_2C_2 systems, respectively. It is important to note that the observed desorption temperatures are lower than ambient temperature, which means most of the H_2 molecules will desorb at room temperature. To address this issue, we plan to enhance the desorption properties by adopting several strategies. Specifically, we aim to investigate the impact of applying an external field or introducing doping techniques to modify the electronic properties of the materials. These approaches could help increase the desorption temperature, thus improving the overall efficiency of the hydrogen storage system. Furthermore, we are also exploring the possibility of the Kubas effect between the H_2 molecules and the metal elements used in the decoration process. This interaction could potentially enhance the binding energy and modify the desorption temperature, offering a pathway to achieve more favorable desorption conditions at or above room temperature.

Finally, in order to evaluate the dynamic stability of both fully loaded systems containing H_2 molecules during the desorption process, we conducted ab initio molecular dynamics (AIMD) simulations in accordance with the desorption temperatures calculated using the van't Hoff equation. The systems under investigation included $32\text{-}8Li@B_2C_2$ and $32\text{-}8Li@B_2CN$, analyzed at temperatures of 100, 200, 400, and 500 K over a simulation duration of 5 ps based on 5000 steps (NSW) with a time step of 1 fs. As illustrated in Fig. 8, the desorption process of the fully loaded systems (side views) reveals that the hydrogen molecules gradually detach from the decorated monolayers as the temperature increases. The desorbed molecules are those with an H_2–Li distance exceeding 2.5 Å, indicating that they have detached from the structure.

Additionally, the radial distribution function (RDF) analysis of $Li@B_2C_2$ and $Li@B_2CN$ systems reveals fundamental insights into their hydrogen storage mechanisms and electronic structure relationships. As it is shown in Fig. 9, the primary Li-H_2 correlation peak at 2.1 Å emerges from specific molecular-level interactions, where the precise d_{Li-H_2} distances (2.24 Å for $Li@B_2C_2$, 2.20 Å for $Li@B_2CN$) reflect optimized coordination geometries that maximize orbital overlap between Li and H_2 molecular orbitals. This optimal geometric configuration facilitates efficient electron density transfer between the Li centers and H_2

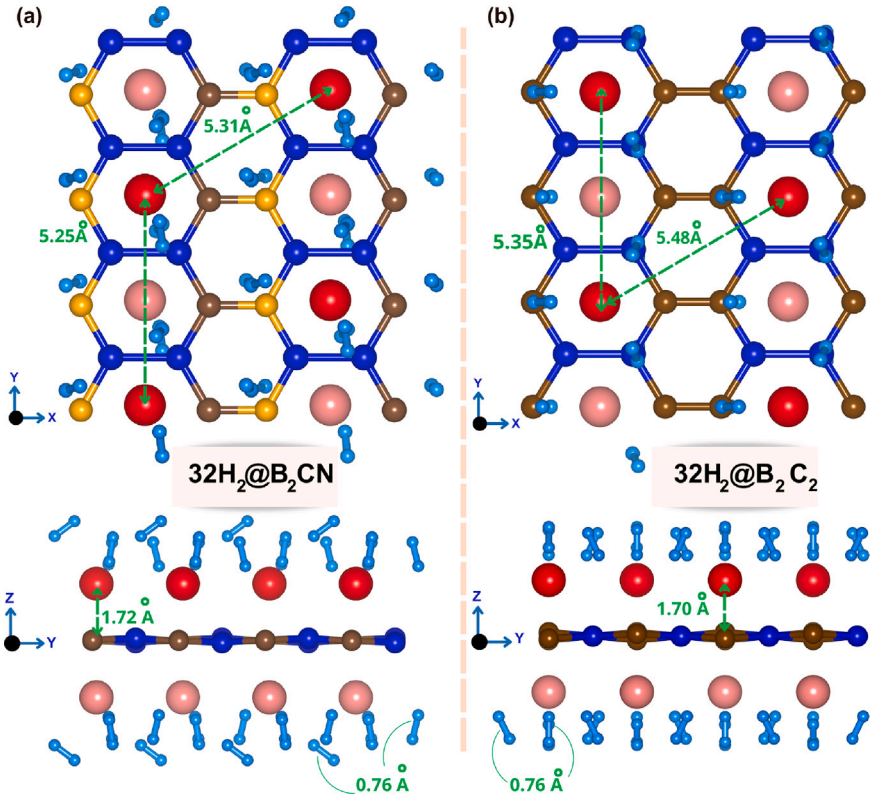

Fig. 6. (a) and (b) Top and side views illustrating the maximum H_2 capture by the 8Li@B_2CN and 8Li@B_2C_2 systems, respectively, along with the distances between lithium atoms, lithium-surface interactions, and the H_2 bond lengths.

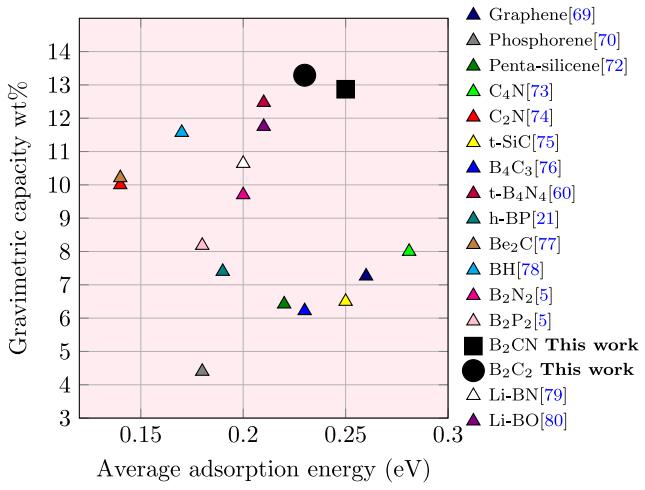

Fig. 7. Comparison of hydrogen storage capacities and average adsorption energies for H_2 molecules adsorbed on 8Li@B_2CN and 8Li@B_2C_2 systems, alongside those of other lithium-decorated 2D materials [5,21,60,69,70,72–80].

molecules, as confirmed by our electronic structure calculations. At low temperatures (100-200K), both systems exhibit well-defined RDF peaks, with Li@B_2C_2 showing a remarkably higher intensity (g(r)≈ 13 at 100 K) compared to Li@B_2CN (g(r)≈ 7 at 100 K). This intensity difference quantitatively correlates with the calculated adsorption energies and electronic density distributions, where the B_2C_2 framework enables more efficient charge transfer to stabilize H_2 molecules. The enhanced electronic interaction in Li@B_2C_2 manifests in the more pronounced RDF features, reflecting stronger spatial correlation and more precise molecular organization of the adsorbed H_2. The emergence of ordered secondary coordination shells at 3.8 Å and 5.9 Å demonstrates long-range molecular organization mediated by the 2D electronic structure, achieving gravimetric capacities of 13.29 wt% for Li@B_2C_2 versus 12.87 wt% for Li@B_2CN through optimized spatial distribution of H2 molecules. These secondary coordination features provide critical insights into the three-dimensional arrangement of H_2 molecules around Li centers, revealing how electronic structure optimization enables higher storage capacity through precise molecular positioning. The temperature-dependent evolution of RDF profiles illuminates the molecular mechanisms of hydrogen desorption and provides quantitative measures of thermal stability. The systematic peak intensity reduction (Li@B_2C_2: g(r) 13→9→6→3.5; Li@B_2CN: 7→5→3→2 from 100 K to 500 K) directly tracks the progressive weakening of Li-H_2 coordination bonds, maintaining the characteristic H-H molecular distance of 0.76 Å throughout the process as evidenced by our MD trajectories. This preservation of the H-H bond length during desorption confirms the molecular nature of the storage mechanism, distinguishing it from dissociative chemisorption processes typical of many metal hydrides. This thermal response manifests through peak broadening and shifts to larger radial distances, where the maintained dH-H indicates molecular hydrogen desorption rather than dissociative processes. The temperature evolution of the RDF profiles provides detailed insights into the desorption pathway, showing how thermal energy progressively overcomes the electronic binding interactions while maintaining molecular integrity. Notably, Li@B_2C_2 preserves higher g(r) values across all temperatures, with g(r) > 3 at 500 K, demonstrating superior kinetic stability derived from its optimized electronic structure. This enhanced thermal stability correlates directly with the more robust electronic interaction between Li centers and the B_2C_2 framework, as evidenced by our electronic structure analysis. The destabilization of Li-H_2 coordination becomes pronounced at 400-500K, yet the persistence of defined correlation peaks in Li@B_2C_2 indicates retention of molecular-scale binding configurations essential for reversible hydrogen storage. The maintenance of structural order at elevated

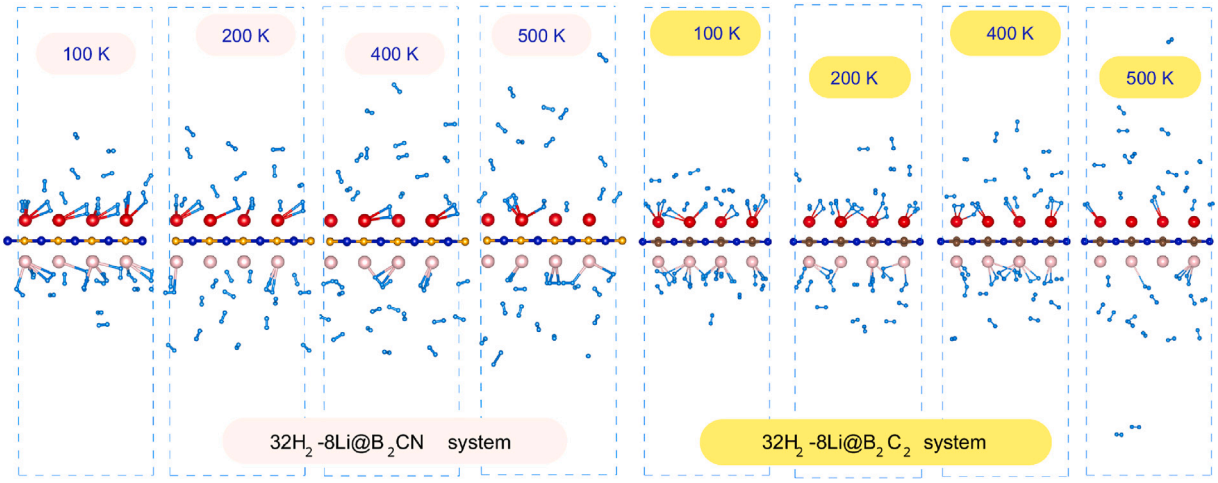

Fig. 8. Side views of 32 H_2 desorbed 8Li@B_2CN and 8Li@B_2C_2 systems. The snapshots are obtained by the end of AIMD calculations for a time scale of 5 ps at T= 100, 200, 400 and 500 K.

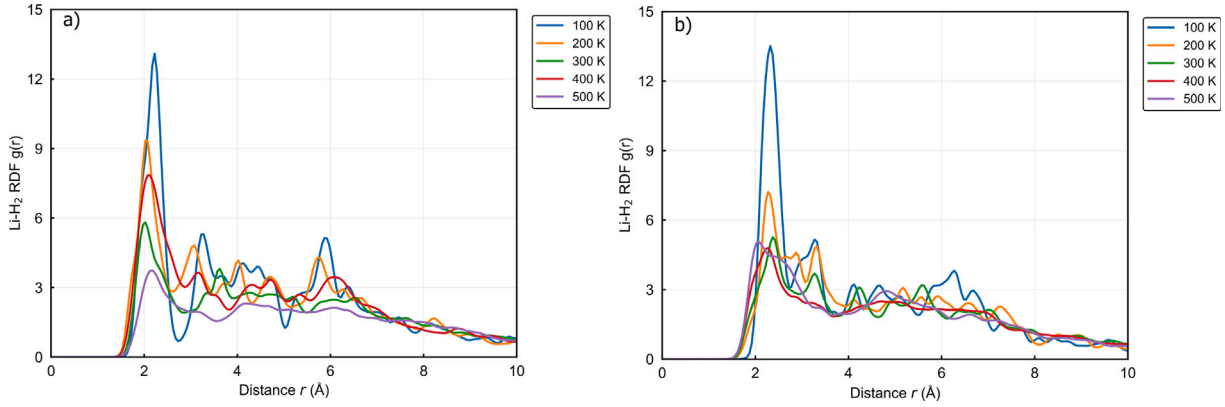

Fig. 9. Radial Distribution Function (RDF) analysis of hydrogen desorption on (a) Li@B_2C_2 and (b) Li@B_2CN systems.

temperatures distinguishes Li@B_2C_2 from typical 2D storage materials, where thermal effects often lead to complete loss of molecular organization. These molecular-level insights establish structure-function relationships governing hydrogen storage performance and provide design principles for next-generation materials. The superior characteristics of Li@B_2C_2 emerge from three synergistic factors: (1) enhanced electronic orbital overlap producing nearly doubled RDF peak intensity at 100 K, directly reflecting stronger Li-H_2 binding interactions, (2) maintenance of coordinated H_2 molecular states up to 500 K evidenced by persistent correlation features, demonstrating exceptional thermal stability, and (3) thermodynamically optimized desorption range of 300-400K aligning with practical operating conditions, ensuring efficient energy utilization in applications. The introduction of nitrogen in B_2CN modifies the electronic density distribution and orbital energetics, quantitatively reflected in reduced RDF intensities and lower desorption temperature thresholds. This electronic structure modification provides valuable insights into how atomic-level compositional changes influence macroscopic storage properties. The preservation of molecular-scale coordination geometry in Li@B_2C_2 through thermal cycling, confirmed by our MD simulations and RDF analysis, establishes a stable platform for repeated adsorption–desorption processes while maintaining the critical electronic and structural features that enable high gravimetric capacity. The remarkable combination of high storage capacity, thermal stability, and reversible operation positions Li@B_2C_2 at the forefront of practical hydrogen storage materials. This comprehensive analysis demonstrates how electronic structure engineering of 2D materials can optimize hydrogen storage properties, establishing Li@B_2C_2 as a promising platform for controlled molecular hydrogen storage with exceptional thermal stability and reversible operation. The clear correlation between electronic structure, molecular organization, and storage performance provides a blueprint for designing future materials with enhanced functionality for clean energy applications.

4. Conclusions

In this study, we explored the potential of 2D orthorhombic B_2C_2 and B_2CN as solid-state materials for hydrogen storage using a lithium decoration strategy. We began by assessing their structural, electronic and mechanical properties, as well as their thermal, dynamic, and thermodynamic stability, which confirmed their suitability for further investigation. Both B_2C_2 and B_2CN demonstrated a strong affinity for lithium, with adsorption energies of −3.72 and −3.38 eV, respectively, values that exceed the cohesive energy of Li atoms, suggesting no risk of cluster formation. Lithium decoration significantly enhanced hydrogen adsorption on both materials compared to their pristine monolayers. For both B_2C_2 and B_2CN, the Li-decorated monolayers (8Li@B_2P_2 and 8Li@B_2N_2) were able to adsorb up to 32 H_2 molecules. The average adsorption energies were found to be 0.23 eV for B_2C_2 and 0.25 eV for B_2CN, corresponding to gravimetric hydrogen storage capacities of 13.29 and 12.87 wt%, respectively, with desorption temperatures of 171 and 186 K. Furthermore, we investigated the desorption process using ab initio molecular dynamics (AIMD) calculations at four different temperatures. The results indicated the reversibility of both systems. Additionally, we conducted a radial distribution function

(RDF) analysis of hydrogen desorption, examining the thermal effects on Li–H atomic correlations and the stability of hydrogen adsorption across various temperatures. Overall, the results indicate that both B_2C_2 and B_2CN possess strong adsorption properties and favorable capacities for hydrogen storage, along with efficient desorption kinetics. These attributes position them as promising candidates for solid two-dimensional materials in hydrogen storage applications.

CRediT authorship contribution statement

Ayoub Benaddi: Writing – original draft, Software, Conceptualization. **Abdelali Elomrani:** Writing – original draft, Data curation, Conceptualization. **Nabil Khossossi:** Writing – review & editing, Software, Investigation. **Mohammad Maymoun:** Writing – original draft, Software, Conceptualization. **Said Oukahou:** Writing – original draft, Software, Conceptualization. **Ayoub Etrini:** Writing – review & editing, Software, Investigation. **Abdellatif Hasnaoui:** Validation, Supervision, Investigation.

Declaration of competing interest

The authors declare that they have no known competing financial interests or personal relationships that could have appeared to influence the work reported in this paper.

Acknowledgments

Part of the simulations conducted in this study were carried out at the CNRST computational center. The authors gratefully acknowledge the support provided by the National Center for Scientific and Technical Research (CNRST) in Morocco.

Appendix A. Supplementary data

Supplementary material related to this article can be found online at https://doi.org/10.1016/j.ijhydene.2025.03.389.

Data availability

All data supporting the conclusions of this research are provided in the main text and Supplementary Material (SM). Additional datasets are available from the corresponding authors upon reasonable request.

References

[1] Khan K, Tareen AK, Aslam M, Zhang Y, Wang R, Ouyang Z, et al. Recent advances in two-dimensional materials and their nanocomposites in sustainable energy conversion applications. Nanoscale 2019;11(45):21622–78.
[2] Chen Y-P, Bashir S, Liu JL. Nanostructured materials for next-generation energy storage and conversion. Springer; 2017.
[3] Sharaf OZ, Orhan MF. An overview of fuel cell technology: Fundamentals and applications. Renew Sustain Energy Rev 2014;32:810–53.
[4] Hou Q, Yang X, Zhang J. Review on hydrogen storage performance of MgH2: development and trends. ChemistrySelect 2021;6(7):1589–606.
[5] Benaddi A, Elomrani A, Lamhani M, Oukahou S, Maymoun M, Fatihi MY, et al. Lithium decorated 2D orthorhombic (o)-B 2 X 2 monolayers for hydrogen storage: first principles calculations. Sustain Energy Fuels 2024;8(8):1719–29.
[6] Khan K, Tareen AK, Aslam M, Wang R, Zhang Y, Mahmood A, et al. Recent developments in emerging two-dimensional materials and their applications. J Mater Chem C 2020;8(2):387–440.
[7] Trivedi R, Kaur S, Garg N, Chakraborty B. Ti-decorated nitrogen-rich BeN4 monolayer for reversible hydrogen storage: DFT investigations. Appl Surf Sci 2023;622:156806.
[8] Elomrani A, Lamhani M, Oukahou S, Sbiaai K, Lebègue S, Hasnaoui A. Two dimensional h-BSb mono-layer as a promising anode material for lithium-ion batteries studied from ab initio simulations. Mater Chem Phys 2022;275:125191.
[9] Maymoun M, Oukahou S, Elomrani A, Lamhani M, Bahou Y, Hasnaoui A, et al. Surface functionalization of penta-siligraphene monolayer for nanoelectronic, optoelectronic and photocatalytic water-splitting: a first-principles study. Appl Surf Sci 2022;590:152972.
[10] Maymoun M, Elomrani A, Oukahou S, Bahou Y, Hasnaoui A, Sbiaai K. Enhancement in photocatalytic water splitting using van der waals heterostructure materials based on penta-layers. Phys Chem Chem Phys 2023;25(4):3401–12.
[11] Elomrani A, Maymoun M, Oukahou S, Lamhani M, Sbiaai K, Hasnaoui A. Evaluating the potential of planar h-BSb monolayer as anode materials for sodium-ion batteries from first principles methods. J Energy Storage 2023;64:107260.
[12] Maymoun M, Oukahou S, Elomrani A, Benaddi A, Etrini A, Ataalite H, et al. Potential application of ternary pentagonal p-SiXY 4 (X=Si, C, Ge; Y= C, B, N) materials for optoelectronics and photocatalytic water splitting: a first-principles study. Sustain Energy Fuels 2024;8(6):1346–57.
[13] Elomrani A, Lamhani M, Oukahou S, Maymoun M, Etrini A, Sbiaai K, et al. Theoretical investigations of layered anode materials. In: Computational design of battery materials. Springer; 2024, p. 437–68.
[14] Bounbaâ M, Khuili M, Fazouan N, Atmani EH, Allaoui I, Houmad M. Li adsorption and diffusion on the surfaces of molybdenum dichalcogenides MoX2 (X=S, Se, Te) monolayers for lithium-ion batteries application: a DFT study. J Mol Model 2023;29(12):378.
[15] Gerstner E. Nobel prize 2010: Andre geim & konstantin novoselov. Nat Phys 2010;6(11):836.
[16] Vogt P, De Padova P, Quaresima C, Avila J, Frantzeskakis E, Asensio MC, et al. Silicene: compelling experimental evidence for graphenelike two-dimensional silicon. Phys Rev Lett 2012;108(15):155501.
[17] Dávila M, Xian L, Cahangirov S, Rubio A, Le Lay G. Germanene: a novel two-dimensional germanium allotrope akin to graphene and silicene. New J Phys 2014;16(9):095002.
[18] Zhu F-f, Chen W-j, Xu Y, Gao C-l, Guan D-d, Liu C-h, et al. Epitaxial growth of two-dimensional stanene. Nat Mater 2015;14(10):1020–5.
[19] Mannix AJ, Zhou X-F, Kiraly B, Wood JD, Alducin D, Myers BD, et al. Synthesis of borophenes: Anisotropic, two-dimensional boron polymorphs. Science 2015;350(6267):1513–6.
[20] Pan C, Zhang J, Kou K, Zhang Y, Wu G. Investigation of the through-plane thermal conductivity of polymer composites with in-plane oriented hexagonal boron nitride. Int J Heat Mass Transfer 2018;120:1–8.
[21] Khossossi N, Benhouria Y, Naqvi SR, Panda PK, Essaoudi I, Ainane A, et al. Hydrogen storage characteristics of Li and Na decorated 2D boron phosphide. Sustain Energy Fuels 2020;4(9):4538–46.
[22] Tian X, Xuan X, Yu M, Mu Y, Lu H-G, Zhang Z, et al. Predicting two-dimensional semiconducting boron carbides. Nanoscale 2019;11(23):11099–106.
[23] Chen X-M, Chen X. Chemical syntheses of two-dimensional boron materials. Chem 2020;6(2):324–6.
[24] Zhao J, Zeng H, Yao G. Computational design of a polymorph for 2D III–V orthorhombic monolayers by first principles calculations: excellent anisotropic, electronic and optical properties. Phys Chem Chem Phys 2021;23(6):3771–8.
[25] Jiang M, Xu J, Munroe P, Xie Z-H. Lithium-decorated SiB monolayer for reversible hydrogen storage: High-capacity realization through strain engineering. Appl Surf Sci 2023;618:156707.
[26] Dai J, Zhao Y, Wu X, Yang J, Zeng XC. Exploration of structures of two-dimensional boron–silicon compounds with sp2 silicon. J Phys Chem Lett 2013;4(4):561–7.
[27] Zhao J, Zeng H, Yao G. Computational design of a polymorph for 2D III–V orthorhombic monolayers by first principles calculations: excellent anisotropic, electronic and optical properties. Phys Chem Chem Phys 2021;23:3771–8. http://dx.doi.org/10.1039/D0CP05909A.
[28] Beniwal S, Hooper J, Miller DP, Costa PS, Chen G, Liu S-Y, et al. Graphene-like boron–carbon–nitrogen monolayers. ACS Nano 2017;11(3):2486–93.
[29] Ci L, Song L, Jin C, Jariwala D, Wu D, Li Y, et al. Atomic layers of hybridized boron nitride and graphene domains. Nat Mater 2010;9(5):430–5.
[30] Cheng M, Chen D, Chen R, Liu W, Lin Q, Zhu Z. Metallized HOT-graphene: A novel reversible hydrogen storage medium with ultrahigh capacity. Int J Hydrog Energy 2023;48(87):34164–79.
[31] Adithya S, Jethawa U, Ali SM, Chakraborty B. Ca-decorated holey graphyne for reversible hydrogen storage: Insights from DFT analysis. Int J Hydrog Energy 2024;90:470–80.
[32] Dewangan J, Mahamiya V, Shukla A, Chakraborty B. Lithium decorated –graphene as a potential hydrogen storage material: density functional theory investigations. Int J Hydrog Energy 2023;48(96):37908–20.
[33] Vaidyanathan A, Mane P, Wagh V, Chakraborty B. Computational design for enhanced hydrogen storage on the newly synthesized 2D polyaramid via titanium and zirconium decoration. ACS Appl Mater & Interfaces 2024;16(7):8589–602.
[34] Pal Y, Lee H, Kaewmaraya T, Aguey-Zinsou K-F, Hussain T, Panigrahi P, et al. Enhanced hydrogen storage properties of light metals dispersed boron hydride monolayer. Int J Hydrog Energy 2024;92:1389–400.
[35] Blöchl PE, Kästner J, Först CJ. Electronic structure methods: Augmented waves, pseudopotentials and the projector augmented wave method. Handb Mater Model: Methods 2005;93–119.
[36] Oukahou S, Elomrani A, Maymoun M, Sbiaai K, Hasnaoui A. Investigation of LiMn1-xMxPO4 (M=Ni, Fe) as cathode materials for Li-ion batteries using density functional theory. Comput Mater Sci 2022;202:111006.
[37] Giannozzi P, Baroni S, Bonini N, Calandra M, Car R, Cavazzoni C, et al. Chiarotti, GLM cococcioni, I. Dabo, et al. J Phys: Condens Matter 2009;21:395502.

[38] Oukahou S, Maymoun M, Elomrani A, Sbiaai K, Hasnaoui A. Enhancing the electrochemical performance of olivine LiMnPO4 as cathode materials for Li-Ion batteries by Ni–Fe codoping. ACS Appl Energy Mater 2022;5(9):10591–603.
[39] Perdew JP, Burke K, Ernzerhof M. D. of physics and NOL 70118 J. quantum theory group tulane university. Phys Rev Lett 1996;77:3865–8.
[40] Oukahou S, Elomrani A, Maymoun M, Sbiaai K, Hasnaoui A. Feeling the strain: Enhancing the electrochemical performance of olivine LiMnPO4 as cathode materials for Li-ion batteries through strain effects. J Energy Storage 2024;75:109663.
[41] Grimme S. Semiempirical GGA-type density functional constructed with a long-range dispersion correction. J Comput Chem 2006;27(15):1787–99.
[42] Mahamiya V, Dewangan J, Chakraborty B. Interplay between van der Waals, Kubas, and chemisorption process when hydrogen molecules are adsorbed on pristine and Sc-functionalized BeN4. Int J Hydrog Energy 2023. http://dx.doi.org/10.1016/j.ijhydene.2023.09.151, URL https://www.sciencedirect.com/science/article/pii/S0360319923047663.
[43] Togo A, Tanaka I. First principles phonon calculations in materials science. Scr Mater 2015;108:1–5.
[44] Lakshmy S, Mane P, Trivedi R, Kalarikkal N, Chakraborty B. Catechol sensing performance of Pd-functionalized two-dimensional polyaramid: A DFT investigation. Langmuir 2024;40(5):2577–90.
[45] Haynes WM. CRC handbook of chemistry and physics. CRC Press; 2016.
[46] Luo X, Yang J, Liu H, Wu X, Wang Y, Ma Y, et al. Predicting two-dimensional boron–carbon compounds by the global optimization method. J Am Chem Soc 2011;133(40):16285–90.
[47] Kaderoglu C, Akturk E, Arkin H. High uptake and fixation ability of BC monolayer for CO and NO toxic gases: a computational analysis [Erratum: November 2021, v. 56 (33), p. 18581]. 2021.
[48] Mortazavi B, Shojaei F, Yagmurcukardes M, Shapeev AV, Zhuang X. Anisotropic and outstanding mechanical, thermal conduction, optical, and piezoelectric responses in a novel semiconducting BCN monolayer confirmed by first-principles and machine learning. Carbon 2022;200:500–9.
[49] Parida AKP. Isoelectronic multiple phases of the carbon-like-biphenylene monolayer of BCN: A first principles study. 2023, arXiv preprint arXiv:2306.08858.
[50] Bafekry A, Naseri M, Fadlallah M, Abdolhosseini Sarsari I, Faraji M, Bagheri Khatibani A, et al. A novel two-dimensional Boron–Carbon–Nitride (BCN) monolayer: A first-principles insight. J Appl Phys 2021;130(11).
[51] Agouri M, Benaddi A, Elomrani A, Khossossi N, Abbassi A, Hasnaoui A, et al. Empowering lithium-ion batteries: The potential of 2D o-Al2N2 as an exceptional anode material through DFT analysis. J Energy Storage 2024;94:112351.
[52] Shin H, Kang S, Koo J, Lee H, Kim J, Kwon Y. Cohesion energetics of carbon allotropes: Quantum Monte Carlo study. J Chem Phys 2014;140(11).
[53] Albe K, Möller W, Heinig K-H. Computer simulation and boron nitride. Radiat Eff Defects Solids 1997;141(1–4):85–97.
[54] Meng L, Ni S, Zhou M, Zhang Y, Li Z, Wu W. Metal–semiconductor transition of two-dimensional Mg 2 C monolayer induced by biaxial tensile strain. Phys Chem Chem Phys 2017;19(47):32086–90.
[55] Hu L, Wu X, Yang J. Mn 2 C monolayer: a 2D antiferromagnetic metal with high Néel temperature and large spin–orbit coupling. Nanoscale 2016;8(26):12939–45.
[56] Li Y, Liao Y, Chen Z. Be2C monolayer with quasi-planar hexacoordinate carbons: a global minimum structure. Angew Chem Int Ed 2014;53(28):7248–52.
[57] Liu H, Neal AT, Zhu Z, Luo Z, Xu X, Tománek D, et al. Phosphorene: an unexplored 2D semiconductor with a high hole mobility. ACS Nano 2014;8(4):4033–41.
[58] Lin H, Liu G, Zhu L, Zhang Z, Jin R, Huang Y, et al. Flexible borophosphene monolayer: A potential Dirac anode for high-performance non-lithium ion batteries. Appl Surf Sci 2021;544:148895.
[59] Khossossi N, Luo W, Haman Z, Singh D, Essaoudi I, Ainane A, et al. Revealing the superlative electrochemical properties of o-B2N2 monolayer in Lithium/Sodium-ion batteries. Nano Energy 2022;96:107066.
[60] EL Kassaoui M, Lakhal M, Benyoussef A, El Kenz A, Loulidi M, Mounkachi O. Improvement of the hydrogen storage performance of t-graphene-like two-dimensional boron nitride upon selected lithium decoration. Phys Chem Chem Phys 2022;24:15048–59. http://dx.doi.org/10.1039/D2CP00480A.
[61] Hussain T, Hankel M, Searles DJ. Graphenylene monolayers doped with alkali or alkaline earth metals: promising materials for clean energy storage. J Phys Chem C 2017;121(27):14393–400.
[62] Mortazavi B, Dianat A, Rahaman O, Cuniberti G, Rabczuk T. Borophene as an anode material for Ca, Mg, Na or Li ion storage: a first-principle study. J Power Sources 2016;329:456–61.
[63] Panigrahi P, Acharya D, Selvi SR, Ahuja R, Hussain T. Enhancing energy storage efficiency of lithiated carbon nitride (C7N6) monolayers under co-adsorption of H2 and CH4. Int J Hydrog Energy 2021;46(38):19988–97.
[64] Li Q-F, Wan X, Duan C-G, Kuo J-L. Theoretical prediction of hydrogen storage on Li-decorated monolayer black phosphorus. J Phys D: Appl Phys 2014;47(46):465302.
[65] Sosa AN, de Santiago F, Miranda Á, Trejo A, Salazar F, Pérez LA, et al. Alkali and transition metal atom-functionalized germanene for hydrogen storage: a DFT investigation. Int J Hydrog Energy 2021;46(38):20245–56.
[66] Wang Y, Zheng R, Gao H, Zhang J, Xu B, Sun Q, et al. Metal adatoms-decorated silicene as hydrogen storage media. Int J Hydrog Energy 2014;39(26):14027–32.
[67] Cabria I, López M, Alonso J. Enhancement of hydrogen physisorption on graphene and carbon nanotubes by Li doping. J Chem Phys 2005;123(20).
[68] Zhang X, Chen F, Jia B, Guo Z, Hao J, Gao S, et al. A novel lithium decorated N-doped 4,6,8-biphenylene for reversible hydrogen storage: Insights from density functional theory. Int J Hydrog Energy 2023;48(45):17216–29. http://dx.doi.org/10.1016/j.ijhydene.2023.01.222, URL https://www.sciencedirect.com/science/article/pii/S0360319923004378.
[69] Seenithurai S, Pandyan RK, Kumar SV, Saranya C, Mahendran M. Li-decorated double vacancy graphene for hydrogen storage application: a first principles study. Int J Hydrog Energy 2014;39(21):11016–26.
[70] Yu Z, Wan N, Lei S, Yu H. Enhanced hydrogen storage by using lithium decoration on phosphorene. J Appl Phys 2016;120(2).
[71] Badzian A, Badzian T, Breval E, Piotrowski A. Nanostructured, nitrogen-doped carbon materials for hydrogen storage. Thin Solid Films 2001;398–399:170–4. http://dx.doi.org/10.1016/S0040-6090(01)01461-4, URL https://www.sciencedirect.com/science/article/pii/S0040609001014614, Proceedings of the 28th International Conference on Metallurgic Coatings and Thin Films.
[72] Zhang Y, Liu P, Zhu X. Li decorated penta-silicene as a high capacity hydrogen storage material: a density functional theory study. Int J Hydrog Energy 2021;46(5):4188–200.
[73] Zhang Y, Liu P, Zhu X, Liu Z. A reversible hydrogen storage material of Li-decorated two-dimensional (2D) C4N monolayer: First principles calculations. Int J Hydrog Energy 2021;46(65):32936–48.
[74] Hashmi A, Farooq MU, Khan I, Son J, Hong J. Ultra-high capacity hydrogen storage in a Li decorated two-dimensional C 2 N layer. J Mater Chem A 2017;5(6):2821–8.
[75] Kassaoui ME, Houmad M, Lakhal M, Benyoussef A, El Kenz A, Loulidi M. Hydrogen storage in lithium, sodium and magnesium-decorated on tetragonal silicon carbide. Int J Hydrog Energy 2021;46(47):24190–201.
[76] Rahimi R, Solimannejad M. Empowering hydrogen storage performance of B4C3 monolayer through decoration with lithium: A DFT study. Surfaces Interfaces 2022;29:101723.
[77] Kassaoui ME, Mansouri Z, Al-Shami A, Sibari A, Benyoussef A, El Kenz A, et al. Design of metal-decorated beryllium carbide (Be2C) as a high-capacity hydrogen storage material with strong adsorption characteristics. Appl Surf Sci 2022;589:152960.
[78] Chen L, Chen X, Duan C, Huang Y, Zhang Q, Xiao B. Reversible hydrogen storage in pristine and Li decorated 2D boron hydride. Phys Chem Chem Phys 2018;20(48):30304–11.
[79] Alfalasi W, Othman W, Hussain T, Tit N. Multifunctionality of vacancy-induced boron nitride monolayers for metal-ion battery and hydrogen-storage applications. Appl Surf Sci 2025;685:162025.
[80] Othman W, Alfalasi W, Hussain T, Tit N. Light-metal functionalized boron monoxide monolayers as efficient hydrogen storage material: Insights from DFT simulations. J Energy Storage 2024;98:113014.